



SCUOLA INTERNAZIONALE SUPERIORE DI STUDI AVANZATI

SISSA Digital Library

Rashba-metal to Mott-insulator transition

Original

Rashba-metal to Mott-insulator transition / Brosco, V., Capone, M.. - In: PHYSICAL REVIEW. B. - ISSN 2469-9950. - 101:23(2020), pp. 1-11. [10.1103/PhysRevB.101.235149]

Availability:

This version is available at: 20.500.11767/126773 since: 2022-03-09T01:03:11Z

Publisher:

Published

DOI:10.1103/PhysRevB.101.235149

Terms of use:

Testo definito dall'ateneo relativo alle clausole di concessione d'uso

Publisher copyright

APS - American Physical Society

This version is available for education and non-commercial purposes.

note finali coverpage

(Article begins on next page)

Rashba-metal to Mott-insulator transition

Valentina Brosco^{1,2} and Massimo Capone²

¹*Istituto dei Sistemi Complessi (ISC-CNR), Via dei Taurini 19, I-00185 Roma, Italy*

²*Scuola Internazionale Superiore di Studi Avanzati (SISSA) and CNR-IOM DEMOCRITOS, Istituto Officina dei Materiali, Consiglio Nazionale delle Ricerche, Via Bonomea 265, 34136 Trieste, Italy*

(Dated: June 17, 2020)

The recent discovery of materials featuring strong Rashba spin-orbit coupling (RSOC) and strong electronic correlation raises questions about the interplay of Mott and Rashba physics. In this work, we employ cluster perturbation theory to investigate the spectral properties of the two-dimensional Hubbard model in the presence of a significant or large RSOC. We show that RSOC strongly favors metallic phases and competes with Mott localization, leading to an unconventional scenario for the Mott transition which is no longer controlled by the ratio between the Hubbard U and an effective bandwidth. The results show a strong sensitivity to the value of the RSOC.

I. INTRODUCTION

The breaking of inversion symmetry has important consequences on the properties of matter. Just to mention few examples, it can lead to unconventional superconducting pairing,^{1,2} it controls magnetic ordering at interfaces and surfaces,³ it rules the generation of spin currents,⁴⁻⁶ and it determines the locking of spin and quasi-momentum in metals with strong Rashba coupling.^{7,8} Furthermore, inversion symmetry breaking effects can be controlled and enhanced by material engineering⁹⁻¹⁴ and gating.^{15,16} In a large class of materials and heterostructures,^{11,13,14,17} inversion symmetry breaking and its effects coexist with electron-electron correlation. This calls for a systematic study of the interplay between these two effects, which, on one hand, can help us to understand parity-violating phenomena in actual solids where interactions are significant and on the other, owing to the intrinsic tendency of correlated systems towards magnetic ordering, holds a huge potential for the development of antiferromagnetic spintronics.^{18,19} Motivated by these findings, in the present work we focus on a well-known consequence of inversion symmetry breaking, namely, Rashba spin-orbit coupling (RSOC),²⁰ and we show that it significantly affects the physics of the metallic and Mott insulating phases and, consequently of the Mott transition connecting the Rashba metal and the Mott insulator. In order to highlight the intrinsic correlation effects, we will restrict to paramagnetic solutions without magnetic ordering.

Previous works describing the interplay of RSOC and electronic correlation were mainly focused on the magnetic phase diagram,^{21,22} on the investigation of topological effects^{23,24} and on the properties of the associated Fermi liquid.^{25,26} Ref.[21] demonstrates that RSOC favors the onset of a metallic phase at weak Hubbard interaction and it modifies the magnetic structure of the insulating phase, in qualitative agreement with a static mean field approach.²²

As a simple approach which allows to study the effects of strong on-site interaction without spoiling the non-abelian gauge structure induced by the SOC, we employ

cluster perturbation theory (CPT). The low-numerical cost of this method allows us to scan a wide region of parameters, ranging from the weakly correlated Rashba metal to the Rashba-Mott insulator phase. We thus investigate two complementary aspects of the interplay of Rashba SOC and electronic correlation. In the Mott insulator phase, we show that, due to the breaking of SU(2) spin symmetry, Rashba SOC yields a mixing of singlet and triplet resonating valence bond (RVB) states possibly opening a new screening channel of local interactions related to the *Pauli screening* discussed in Ref. [27]. At large Rashba coupling and strong interaction where the system realizes a correlated metallic phase, we instead demonstrate that the breaking of parity associated with Rashba SOC enables two kinds of low-energy fermionic excitations and it results in a pseudogap phase. In both metallic and insulating phases we find that RSOC counteracts localization effects, yielding qualitative and quantitative modifications in the Mott transition. Our work thus hints at an enhancement of transport in strongly correlated systems in the presence of RSOC, opposite to what happens in weakly interacting disordered Fermi gases.²⁸⁻³⁰ It can be therefore extremely relevant to account for the transport properties of oxides heterostructures,³¹ surface alloys¹¹ and polar semiconductors.^{14,17,32} Furthermore it suggests the possibility of exploiting the tunability of Rashba spin-orbit coupling to control transport in strongly correlated materials.

The paper is organized as follows. After describing the model and the method in Section II, in Section III we present our main results concerning the structure of the spectrum and the density of states across the metal-insulator transition. We then discuss the peculiarities of the Rashba-Mott insulator in Section III A while in section III B we focus on the correlated metallic phase. Eventually in the Appendices we discuss technical details on the method.

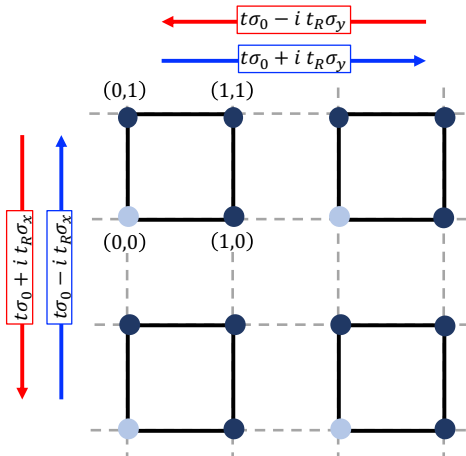


FIG. 1: Plaquette tiling of the square lattice. Both intra and inter plaquette tunneling include a standard spin-diagonal and a spin dependent tunneling. Inter-plaquette tunneling is treated perturbatively.

II. MODEL

We consider the following Rashba-Hubbard model

$$H = H_0 + H_U. \quad (1)$$

where H_U is the Hubbard interaction,

$$H_U = U \sum_i n_{i\uparrow} n_{i\downarrow}, \quad (2)$$

while H_0 can be written as the sum of a standard spin-diagonal hopping and a spin-flip Rashba hopping term between nearest-neighboring sites as follows

$$H_0 = -t \sum_{\langle ij \rangle} c_i^\dagger c_j - t_R \sum_{\langle ij \rangle} c_i^\dagger (\vec{\alpha}_{ij} \times \vec{\sigma})_z c_j \quad (3)$$

where we introduced the local spinor creation and annihilation operators c_i^\dagger and c_i and we defined the vector $\vec{\alpha}_{ij} = (\alpha_{ij}^x, \alpha_{ij}^y)$ with $\alpha_{ij}^\mu = i(\delta_{ij+a_\mu} - \delta_{ij-a_\mu})$ where a_μ is the unitary translation in the μ direction.

We use cluster perturbation theory^{33,34} (CPT) as a simple and computationally extremely cheap method which is able to capture the competition between the inherently non-local physics described by H_0 and the local interaction H_U which drives the system towards Mott localization.

Within this approach the lattice is partitioned into a superlattice of identical clusters and the Green's function $G(\omega, \mathbf{k})$ is computed solving exactly the cluster and, treating the intercluster hopping perturbatively. Specifically, we use four-site plaquette clusters that, as stressed in Ref.[27], are the minimal clusters where the non-abelian gauge structure of Rashba coupling can emerge. With this choice, our study encompasses the Pauli screening mechanism discussed in Ref.[27] and it preserves the basic symmetries of the lattice.

We tile the lattice as shown in Fig. 1. and we decompose the lattice vectors as $\mathbf{r}_i = \mathbf{r}_m + \mathbf{r}_a$ where \mathbf{r}_m enumerates the plaquette superlattice sites (light-blue dots in Fig. 1) and it refers to the position of the lowermost left site of each plaquette while \mathbf{r}_a indicates the position of the site in the plaquette. The Hamiltonian is thus partitioned as follows:

$$H = H_{\text{loc}} + V \quad (4)$$

where H_{loc} contains all the intra-cluster terms (diagonal in the index m) including interaction while V accounts for the interplaquette hopping. The matrix V and the local Hamiltonian are defined to guarantee current conservation upon tunneling along x and y . In particular, as schematically indicated by the blue and red arrows in Fig. 1 tunneling in opposite directions yields opposite spin rotations. More details on the partitioning are given in Appendix A.

Following the route suggested e.g. in Ref. [34], we perform a partial Fourier transformation with respect to the cluster position indices describing the Hamiltonian H in the mixed representation.

In this representation V can be recast as follows

$$V = - \sum_{\mathbf{k}, a, b} c_{a\mathbf{k}}^\dagger \tilde{T}_{ab}(\mathbf{k}) c_{b\mathbf{k}}. \quad (5)$$

where \mathbf{k} belongs to the Brillouin zone of the original lattice while the interplaquette hopping amplitude $\tilde{T}_{ab}(\mathbf{k})$ is represented by a 2×2 matrix spin space. The full interplaquette hopping matrix has thus dimension 8 and it can be written as follows

$$\tilde{T}(\mathbf{k}) = (e^{-2ik_x}(t\sigma_0 + it_R\sigma_y) \otimes \tau_x + e^{-2ik_y}(t\sigma_0 - it_R\sigma_x) \otimes \tau_y + \text{H.c.}) \quad (6)$$

with the matrices τ_x and τ_y denoting forward unitary translations in the x and y direction in the plaquette. Starting from Eqs.(4-6) we obtain the following expression for the Green's function of the lattice

$$G(\omega, \mathbf{k}) = \frac{1}{4} \sum_{a, b} \tilde{g}_{ab}(\omega, \mathbf{k}) e^{i\mathbf{k} \cdot (\mathbf{r}_a - \mathbf{r}_b)} \quad (7)$$

where a and b enumerate the sites in the plaquette and $\tilde{g}_{ab}(\omega, \mathbf{k})$ is a 2×2 matrix in spin-space denoting the single-particle Green's function of H to lowest order in the interplaquette hopping V ³⁵ i.e.

$$\tilde{g}(\omega, \mathbf{k}) = [g_{\text{loc}}^{-1}(\omega) - \tilde{T}[\mathbf{k}]]^{-1} \quad (8)$$

where $g_{\text{loc}}(\omega)$ is the exact plaquette's Green's function. The overall structure of the spectrum can be then deduced from the spectral function, $A_0(\omega, \mathbf{k})$, defined as $A_0(\omega, \mathbf{k}) = -\frac{1}{2\pi} \text{Im Tr} [G(\omega, \mathbf{k})]$ while the spin-polarization of the states can be described using the spin-projected spectral function $A_\mu(\omega, \mathbf{k}) = -\frac{1}{2\pi} \text{Im Tr} [G(\omega, \mathbf{k}) \sigma_\mu]$ with $\mu = x, y, z$.

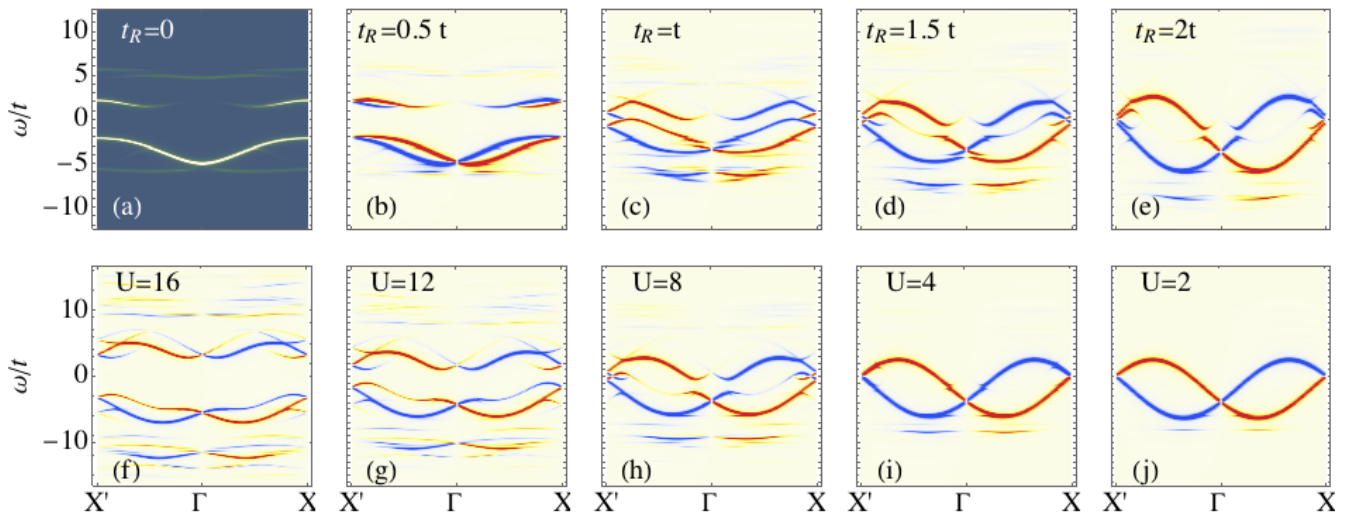


FIG. 2: Evolution of the spectrum across the Mott transition along the axis k_x , red and blue colors indicate positive and negative y -polarization. Mott insulating phases for weak and strong spin-orbit are shown on the upper and lower leftmost panels while metallic phases for, respectively, strong and weak interaction are shown on the rightmost panels. Specifically, upper panels, (a-e), show $A_y(\omega, \mathbf{k})$ for $t_R \in [0, 2t]$ and $U = 6t$ while lower panels, (f-j), show $A_y(\omega, \mathbf{k})$ for $t_R = 2t$ and $U \in [16t, 2t]$.

III. METAL-INSULATOR TRANSITION IN THE PRESENCE OF RASHBA SOC

We start by presenting the evolution of the spectrum along two representative lines in the space of parameters which cross the insulator-to-metal transition starting from the insulating solution. In particular, the first row of Fig.2 (Panels (a-e)) shows results for fixed $U = 6t$ and increasing values of the Rashba coupling t_R , while in the second row (Panels (f-j)) we fix a moderately large value of the RSOC $t_R = 2t$ and we vary U ranging from $U = 16t$ to $U = 2t$. To trace the modifications and merging of the different bands we focus on the structure of the spectrum along the line $X'-\Gamma-X$, with $X = (\pi, 0)$, $\Gamma = (0, 0)$ and $X' = (-\pi, 0)$ and we plot the σ_y -component of the spectral function, $A_y(\omega, \mathbf{k})$.

In the absence of RSOC ($t_R = 0$), (Fig. 2a), CPT yields a spectral functions featuring two well-defined Hubbard bands along with two satellite bands, similar results were obtained in Ref.[33] As we switch on a small Rashba coupling, the Hubbard bands acquire an helical structure, as shown in Fig. 2b and discussed in more details in Appendix A. A further increase of t_R then induces a transition to a metallic state, (Fig.2(c-d)) and, in the limit of large t_R the spectrum strongly resembles the non-interacting one Figs.2(e,i,j). Therefore, as t_R

goes from $0.5t$ to $2t$ the system undergoes a transition from a Mott insulator with spin-split Hubbard bands to a Rashba metal despite the interaction is unchanged to $U = 6t$.

On the other hand, if we start from a Rashba metal with a large value of Rashba SOC, shown in Fig.2(h), and we increase Hubbard interaction strength we can drive the system towards an insulating phase, realized at large t_R and strong interaction, that differs significantly from the weak-SOC Mott-insulator shown in Fig. 2(b). As one can see in Fig. 2(f), where we show the spectral function for $U = 16t$ and $t_R = 2t$, this strong-SOC insulating phase is characterized by a flat spectrum with a very weak \mathbf{k} dependence. When U is reduced, the non-interacting band-structure is recovered by merging the outer branches of the two bands, *i.e.* the positive helicity branch of the upper Hubbard band and the negative helicity branch of the lower Hubbard band. The inner branches progressively disappear across the transition as shown in Fig. 2(f-j).

A. Mott-Rashba insulators

To elucidate the nature of the insulating phases realized at small and large t_R we recall that while at $t_R = 0$

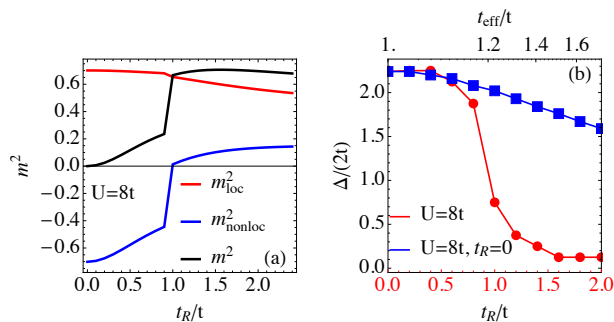


FIG. 3: (a) Local and non-local magnetization as defined by Eqs.(11-12) as a function of t_R for $U = 8t$. (b) Red line: Mott gap as a function of the ratio t_R/t shown on the lower horizontal scale for $U = 8t$. Blue line: Mott gap for $t_R = 0$, $U = 8t$ and a diagonal tunneling amplitude t_{eff} , shown on the upper horizontal scale.

Lieb's theorem³⁶ prescribes zero total magnetic moment, *i.e.*

$$\langle S^2 \rangle = \langle S_x^2 + S_y^2 + S_z^2 \rangle = 0 \quad (9)$$

with $S_\mu = \sum_i c_i^\dagger \sigma^\mu c_i$, at $t_R \neq 0$ the breaking of the $SU(2)$ spin symmetry removes the constraint on S^2 that acquires a finite value. It is then useful to cast the average squared magnetization, $m^2 = \langle S^2 \rangle / L$, where L is the number of sites, as the sum of a local and a non-local contribution,

$$m^2 = m_{\text{loc}}^2 + m_{\text{nonloc}}^2. \quad (10)$$

In the above equation m_{loc}^2 quantifies the local magnetic moment and it can be easily related to the average double occupancy, $d = 1/L \sum_i \langle n_{i\uparrow} n_{i\downarrow} \rangle$ and to the density per site n ,

$$m_{\text{loc}}^2 = \frac{1}{L} \sum_{\mu,i} \langle (c_i^\dagger \sigma^\mu c_i)^2 \rangle = 3(n - 2d) \quad (11)$$

while m_{nonloc}^2 characterizes the spin-spin correlation between different sites:

$$m_{\text{nonloc}}^2 = \frac{1}{L} \sum_{\mu,i \neq j} \langle (c_i^\dagger \sigma^\mu c_i) (c_j^\dagger \sigma^\mu c_j) \rangle. \quad (12)$$

From Eqs. (11) and (12) it follows that in the standard Hubbard model with $t_R = 0$ the decrease of the double occupancy driven by the interaction is unavoidably associated to the creation of negative non-local spin correlations; the constraint $m^2 = 0$ indeed implies $m_{\text{nonloc}}^2 = -m_{\text{loc}}^2$. On the other hand, the presence of a finite Rashba coupling removes the constraint $m^2 = 0$ and it allows m_{nonloc}^2 and m_{loc}^2 to vary independently.

This is clearly shown in Fig.3(a) where we plot the local and non-local magnetization as well as their sum, approximated using the single-cluster ground-state, as a

function of t_R/t for $U = 8t$. There are two fundamentally different regimes: the first, realized at small t_R , is characterized by $m_{\text{nonloc}}^2 < 0$ corresponding to predominant antiferromagnetic (AF) correlations, in this regime we recover the standard result $\langle S^2 \rangle = 0$ at $t_R = 0$, the second regime, realized at large t_R , is instead characterized by $m_{\text{nonloc}}^2 \gtrsim 0$ indicating predominantly helical (HL) correlations.³⁸

A natural question that arises here is whether the onset of the HL regime affects the metal-insulator transition. To answer this question, in Fig.3(b) we plot the Mott gap as a function of t_R/t for $U = 8t$ and we compare it with the gap of a Hubbard model having the same bandwidth but no RSOC, *i.e.* with a standard square lattice Hubbard model having an effective spin-diagonal hopping amplitude, $t_{\text{eff}} = \sqrt{t + t_R^2}/2$.³⁹ We see that the onset of the HL regime brings about a change in the behavior of the Mott gap that becomes strongly sensitive to the ratio of t_R/t and it falls rapidly to zero. On the contrary, in the absence of Rashba SOC, we obtain a much weaker dependence on the ratio U/t_{eff} . Including dynamic correlations neglected by CPT, or increasing the cluster size will probably reduce the gap but it will not qualitatively modify its behavior, as briefly outlined in Appendix A 3. These results suggest that the metal-insulator transition is then not simply driven by the decrease of the double occupancy, controlled by the ratio U/t_{eff} , but it also depends on the strength and nature of non-local spin correlations. Further evidences in this direction may be found in appendix B where we compare the effects Rashba coupling and of next-nearest-neighbour tunneling on the charge gap. There we show that, although the latter kind of hopping destroys the nesting and reduces the density of states at the Fermi level, its overall effect on the charge gap is rather different from that of RSOC for moderate and large values. The presence of Rashba spin-orbit coupling thus seems to favor metallic phases and to introduce new screening mechanisms. A somewhat similar situation is realized in the presence of Hund's coupling in multiorbital systems where more than one orbital is available on every lattice site. Here the role of non-local spin correlations is played by the orbital magnetization.⁴⁰ Our analysis also shows that the effect of Rashba coupling differs from that of an external constant magnetic field despite a superficial similarity. In this simpler case, the total magnetic moment increases as a function of the magnetic field strength, mostly due to an increase of the local magnetization, while Rashba SOC instead mostly affects the non-local magnetization. This leads to a basic and important difference in the limit of very large couplings. Obviously very large magnetic fields drive the system towards a band insulator⁴¹ while a very large Rashba SOC leads to a semimetallic state, as we discuss in more details in the following Section.

Before proceeding further let us add a technical remark. We extract the gap from the density of states. In order to obtain a numerical estimate, we use twice the energy of the first point where the density of states

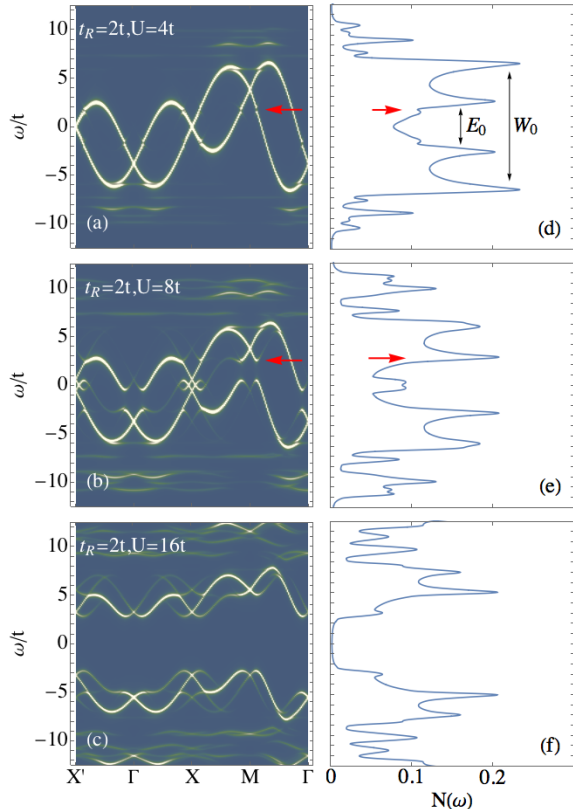


FIG. 4: Evolution of the spectral function $A_0(\omega, \mathbf{k})$ across the Mott transition for $t_R = 2t$ and $U \in [4t, 16t]$, Lorentzian broadening $\eta = 0.1t$ in the spectral function plots and $\eta = 0.25t$ in the DOS plots. The red arrows in panels (a,d) signal rifts in the spectral function and the corresponding peaks in the DOS.

changes curvature from positive to negative (the factor two comes from the symmetry around zero energy of the DOS). As one can easily understand by looking at Fig.4 for each value of t_R , this procedure yields the “true” gap and not the pseudogap.

B. Correlated Rashba metal

As one can see in Fig.2(d,h), a peculiarity of the Mott transition in the presence of Rashba SOC is that at the transition the spectrum remains ungapped around the X and $Y = (0, \pi)$ points while a pseudogap appears around Γ and $M = (\pi, \pi)$ points in the first Brillouin zone. This behavior can be qualitatively understood considering that the Rashba spin-orbit coupling introduces Fermi-level Dirac crossings at the X and Y points. Low-energy fermions with momentum close to the X and Y points therefore behave as nodal fermions and they are more robust to interaction effects as compared to the

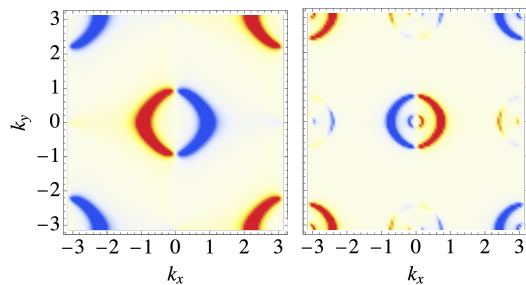


FIG. 5: Spin-polarized spectral function, $A_y(\omega, \mathbf{k})$, at the Fermi level, $\omega = 0$, for $t_R = 2t$ and $U = 0$ (left) and $t_R = 2t$ and $U = 8t$ (right).

standard fermions present around Γ and M points.

Signatures of the presence of two kinds of fermionic quasi-particles behavior may be also found in the density of states shown in Fig.4. There we see that in the weakly correlated phase, shown in Fig.4(a), the spectrum bears strong similarities with the non-interacting one. In particular, due to the presence of Rashba coupling, the Van Hove singularity at $\omega = 0$ characteristic of two-dimensional square lattices is split into two peaks separated by an energy $E_0 = 4t(\sqrt{1 + t_R^2/t^2} - 1)$. At the same time two additional van-Hove singularities appear at the band edges with a distance proportional to the non-interacting bandwidth $W_0 = 8t\sqrt{1 + t_R^2/(2t^2)}$. The signatures of correlation, in this case, are the transfer of spectral weight at large ω associated with spin-wave excitations and the appearance of rifts at the points Γ and M yielding the two small peaks close to the Fermi level indicated with a red arrow in Fig. 4(a). As we increase interaction, the rifts evolve into a pseudogap (Fig. 4(b)) and two additional peaks appear associated with the opening of the gap at the points X and Y. This intermediate regime is characterized by a Fermi surface shown in Fig. 5 consisting of two circles centered at the Γ and M points with two additional pockets appearing at the points X and Y and displaying a complex spin texture reminiscent of that recently found in Ref.[42].

Fig. 4(c) shows the DOS in the insulating phase. In this phase the four-peak structure characteristic of the non-interacting Rashba metal on the square lattice is reproduced in each of the two Hubbard bands. However, the changes in the bands dispersion induced by Hubbard interaction, clearly visible in Fig. 4(c), demonstrate a non-trivial renormalization of the different contributions to the kinetic energy. We notice that cluster-Dynamical Mean-Field Theory studies of the two-dimensional Hubbard models have shown similar physics where the interactions give rise to different renormalizations of nearest-neighbor and further-range hoppings, leading to renormalizations of the Fermi surface⁴³ and appearance of the pseudogap and the superconducting gap⁴⁴.

IV. CONCLUSIONS

In this manuscript we have studied the interplay between a sizable Rashba spin-orbit coupling and Hubbard-like local interactions in a two-dimensional lattice model. We find that the presence of RSOC deeply affects the Mott transition and it has two crucial effects: (i) it makes local and non-local magnetization independent, in contrast with the pure Hubbard model, where the formation of large local magnetic moments leads to negative non-local spin correlations and (ii) it introduces robust nodal quasiparticles. As a consequence, the RSOC strongly favors metallic phases, turning a Mott insulator into a Rashba metal through a transition which can not be described in terms of an effective standard Hubbard model with a renormalized kinetic term. The spectral properties reveal different mechanism in which the insulator transforms into a metal and underline a strong sensitivity of the spectral and transport properties on the value of the ratio between the RSOC and the standard hopping amplitude. Our results provide the community with simple and practical information about the strong effect of the spin-orbit coupling on Mott localization, which can be used as the cornerstone for the study of systems featuring simultaneously large RSOC and large Hubbard U and as guidelines to tune and tailor the properties of these systems. To be concrete, let us discuss in more detail the connection with two recent experimental works which are pioneering the field of strongly correlated Rashba systems, reported in Refs. [11] and [42].

In Ref.[11] Tresca *et al.* investigate the 1/3 monolayer α -Pb/Si(111) by scanning tunneling microscopy finding a metallic ground state in sharp contrast to what happens e.g. in Sn on Si(111) that is a Mott insulator.⁴⁵ By detailed first principle calculations including on equal footing relativistic and correlation effects they show that a peculiar feature of the former system is the strong spin-orbit coupling. Despite our simple single-band square-lattice Rashba-Hubbard model cannot fully describe the complexity of α -Pb/Si(111), a simple analysis of the results of Ref.[11] shows that their parameters are in a regime where Pauli screening is relevant. Surface-band electrons indeed experience a very strong Hubbard interaction and a significant spin-orbit splitting of about 25% of the bandwidth which in our model would correspond to $t_R \sim 1.5t$.

In Ref. [42], the author unveil the spin-texture of the Fermi surface of the cuprate superconductor Bi2212 by spin-resolved ARPES. We already noticed that a similar spin-texture arises within our model.

The present work also triggers a number of interesting questions concerning the effects of inversion symmetry breaking and Rashba spin-orbit coupling on superconductivity in strongly correlated systems. In fact, while it is well-known that Rashba coupling may enhance electron-phonon superconductivity⁴⁶ the effects of spin-orbit coupling on high- T_c and unconventional superconductors are still to a large extent unknown².

V. ACKNOWLEDGEMENTS

We are grateful to A. Amaricci for precious discussions. We acknowledge support from the H2020 Framework Programme, under ERC Advanced GA No. 692670 FIRSTORM and from MIUR PRIN 2015 (Prot. 2015C5SEJJ001) and SISSA/CNR project ‘Superconductivity, Ferroelectricity and Magnetism in bad metals’ (Prot. 232/2015).

Appendix A: Cluster perturbation theory in the presence of Rashba spin-orbit coupling

The general idea of cluster perturbation theory^{34,47} (CPT) is to construct an approximate solution for interacting lattice models starting from the exact solution of individual clusters of sites by means of a perturbation theory in the intercluster hopping.

This statement already contains essential information concerning CPT, *i.e.* (i) it is a perturbation theory in the hopping and as such it is delicate since the reference system is interacting; (ii) it is controlled to some extent by the cluster size, L_c , since it becomes trivially exact in the limit $L_c \rightarrow \infty$ and, as shown e.g. in Ref.[48] it reduces to the Hubbard I approximation for $L_c = 1$.

The derivation of CPT equations can be done in several ways by means of diagrammatic perturbation theory⁴⁹ or path integral approaches.⁴⁷ Here we briefly outline the path integral derivation illustrating the differences arising due to the presence of Rashba spin-orbit coupling^{8,20} (SOC).

1. Model and Hamiltonian partitioning

The model is described by the following Hamiltonian:

$$H = H_0 + H_U \quad (\text{A1})$$

where H_U denotes the Hubbard interaction,

$$H_U = U \sum_i n_{i\uparrow} n_{i\downarrow} \quad (\text{A2})$$

while H_0 indicates the non-interacting Hamiltonian and it includes a spin-diagonal hopping proportional to t and a spin-dependent hopping quantified by t_R associated with Rashba spin-orbit coupling. Introducing the spinor creation and annihilation operators $c_i^\dagger = (c_{i\uparrow}^\dagger, c_{i\downarrow}^\dagger)$ and $c_i = (c_{i\uparrow}, c_{i\downarrow})$, the Hamiltonian H_0 can be cast as follows

$$H_0 = \sum_{ij} c_i^\dagger [t \sigma_0 \Delta_{ij} + t_R (\vec{\alpha}_{ij} \times \vec{\sigma})_z] c_j \quad (\text{A3})$$

where i enumerates the sites of 2D square lattice, Z_γ , $\vec{\sigma}$ denotes the vector of Pauli matrices, $\vec{\alpha} = (\alpha_{ij}^x, \alpha_{ij}^y, 0)$ and

$\alpha_{ij}^\mu = i(\delta_{ij+\eta_\mu} - \delta_{ij-\eta_\mu})$ and $\Delta_{ij} = \sum_\mu (\delta_{ij+\eta_\mu} + \delta_{ij-\eta_\mu})$ with η_x and η_y denoting the unit vectors (1,0) and (0,1).

The first step to construct a CPT consists in tiling the lattice with small clusters whose Hamiltonian can be diagonalized exactly. As clusters we use 2×2 plaquettes: this choice has preserves the symmetries of the lattice and allows to easily account for the chiral structure of Rashba SOC. Furthermore, thanks to the small clusters size, it allows the investigation of a wide region of parameters with small computational efforts.

The clusters superlattice, Z_Γ , is defined by decomposing the vectors of the original lattice, Z_γ , as follows

$$\mathbf{r}_i = \mathbf{r}_m + \mathbf{r}_a \quad (\text{A4})$$

where \mathbf{r}_m denotes the position of the lowermost left site of each plaquette while \mathbf{r}_a indicates the position of the site inside the plaquette. Therefore, $\mathbf{r}_m = (m_x a_x, m_y a_y)$ with m_x and m_y even numbers and $\mathbf{r}_a = (\beta_x a_x, \beta_y a_y)$ with $\beta_x, \beta_y \in [0, 1]$ and a_μ denote the primitive lattice vectors.

Using the map defined in Eq.(A4) we can easily rewrite the hopping Hamiltonian as follows:

$$H_0 = - \sum_{m,n,a,b} c_{am}^\dagger T_{am,bn} c_{bn}. \quad (\text{A5})$$

where $T_{am,bn} = T_{am,bn}^x + T_{am,bn}^y$ is a matrix in spin-space that describes the hopping of one electron from site b of cluster n to site a of cluster m . The structure of the hopping matrix, $T_{am,bn}$, can be most easily understood by looking at Fig.6. There we see that, given the map defined in Eq.(A4), forward (backward) interplaquette tunneling is associated with backward (forward) translation of the intracluster indices. In the presence of Rashba SOC this leads to the following expression for the tunneling along x

$$T_{am,bn}^x = (\delta_{m,n+2\eta_x} \delta_{a,b-\eta_x} + \delta_{m,n} \delta_{a,b+\eta_x}) [t\sigma_0 + i t_R \sigma_y] + (\delta_{m,n-2\eta_x} \delta_{a,b+\eta_x} + \delta_{m,n} \delta_{a,b-\eta_x}) [t\sigma_0 - i t_R \sigma_y] \quad (\text{A6})$$

and for the tunneling along y

$$T_{am,bn}^y = (\delta_{m,n+2\eta_y} \delta_{a,b-\eta_y} + \delta_{m,n} \delta_{a,b+\eta_y}) [t\sigma_0 - i t_R \sigma_x] + (\delta_{m,n-2\eta_y} \delta_{a,b+\eta_y} + \delta_{m,n} \delta_{a,b-\eta_y}) [t\sigma_0 + i t_R \sigma_x]. \quad (\text{A7})$$

Starting from the above equations it is straightforward to partition the Hamiltonian as

$$H = H_{\text{loc}} + \hat{V} \quad (\text{A8})$$

where V describes the inter-cluster hopping while H_{loc} contains all intra-cluster terms.

Specifically, arranging the creation and annihilation operators on a given cluster in a vectorial form, \hat{V} can be written as

$$\hat{V} = - \sum_{m \neq n} C_m^\dagger V_{m,n} C_n \quad (\text{A9})$$

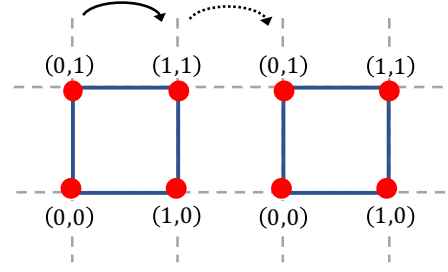


FIG. 6: The solid and dotted lines show examples of forward intra- and inter- plaquette tunneling along x .

with $V_{m,n} = V_{m,n}^x + V_{m,n}^y$ and e.g. $V_{m,n}^x$ given by

$$V_{m,n}^x = \delta_{m,n-2\eta_x} \tau_x^+ \otimes (t\sigma_0 - i t_R \sigma_y) + \delta_{m,n+2\eta_x} \tau_x^- \otimes (t\sigma_0 + i t_R \sigma_y) \quad (\text{A10})$$

where τ_μ^+ (τ_μ^-) denote a single-site forward (backward) translation in the μ direction of the intra-cluster indices. Similarly, H_{loc} can be cast as

$$H_{\text{loc}} = - \sum_m C_m^\dagger T' C_m + H_U \quad (\text{A11})$$

with

$$T' = \tau_x^+ \otimes (t\sigma_0 + i t_R \sigma_y) + \tau_x^- \otimes (t\sigma_0 - i t_R \sigma_y) + \tau_y^+ \otimes (t\sigma_0 - i t_R \sigma_x) + \tau_y^- \otimes (t\sigma_0 + t_R \sigma_x). \quad (\text{A12})$$

From the above equations we see that the presence of Rashba coupling leads to a redefinition of the local Hamiltonian and of the inter-cluster hopping. Both these terms acquire a spinorial structure and are described by matrices of dimension $2L_c$ where L_c denotes the cluster size.

2. Path integral derivation of CPT equations

The purpose of this section is to present a schematic derivation of the CPT relation between cluster and lattice Green's functions, Eq. (7-8) of section II, using a path integral approach.

We start by introducing the vectors of Grassman fields Γ_m and Γ_m^* corresponding to the vectors of fermion operators C_m and C_m^\dagger and we write the partition function as

$$Z = \int \mathcal{D}(\Gamma_m^*, \Gamma_m) \exp \left[- \int_0^\beta (\Gamma_m^* \partial_\tau \Gamma_m + H_{\text{loc}}) d\tau \right] \cdot \exp \left[\int_0^\beta \Gamma_m^* V_{mn} \Gamma_n d\tau \right] \quad (\text{A13})$$

where we follow the notation of Ref.[50] and the sum over repeated indices in the exponent is implied. Following the

route outlined in Refs.[34,47,48], we perform a Grassmannian Hubbard-Stratonovich transformation and recast the partition function as a Gaussian integral over

$$Z = \det V \int \mathcal{D}(\Gamma_m^*, \Gamma_m) \mathcal{D}(\Psi_m^*, \Psi_m) \exp \left[- \int_0^\beta (\Gamma_n^* \partial_\tau \Gamma_n + H_{\text{loc}}) d\tau \right] \exp \left[\int_0^\beta (\Psi_m^* V_{mn}^{-1} \Psi_n + \Psi_n^* \Gamma_n + \Gamma_n^* \Psi_n) d\tau \right]. \quad (\text{A14})$$

We see that the Γ -fields action is completely local, this allows to factorize the Γ -integral and arrive at the following expression for the partition function

$$Z = \det V Z_0 \int \mathcal{D}(\Psi_m^*, \Psi_m) \exp \left[\int_0^\beta \Psi_m^* V_{mn}^{-1} \Psi_n d\tau \right] \cdot \exp \left[\sum_m S_m(\Psi_m^*, \Psi_m) \right] \quad (\text{A15})$$

where $Z_0 = \prod_m z_m^0$ denotes the local partition function, i.e. $z_m^0 = \int \mathcal{D}(\Gamma^*) e^{-S_{\text{loc}}}$ with $S_{\text{loc}} = \int_0^\beta (\Gamma_n^* \partial_\tau \Gamma_n + H_{\text{loc}}) d\tau$, while $S_m(\Psi_m^*, \Psi_m)$ is defined as follows

$$S_m(\Psi_m^*, \Psi_m) = \log \left(\langle e^{-\int_0^\beta (\Psi_m^* \Gamma_m + \Gamma_m^* \Psi_m) d\tau} \rangle_0 \right) \quad (\text{A16})$$

where the subscript 0 indicates averages with a local statistical weight $\langle \dots \rangle_0 = 1/Z_0 \int \mathcal{D}(\Gamma^*) \dots e^{-S_{\text{loc}}(\Gamma, \Gamma^*)}$. Starting from Eq.(A16) and expanding the exponential yields a complicate interacting theory for the auxiliary fields: CPT consists in keeping only the first order of this expansion setting

$$S_m(\Psi_m^*, \Psi_m) \simeq - \int_0^\beta d\tau_1 d\tau_2 \psi_m^*(\tau_1) G_{\text{loc}}(\tau_1 - \tau_2) \psi_m(\tau_2) \quad (\text{A17})$$

where $G_{\text{loc}}(\tau_1 - \tau_2)$ denotes the cluster Green's function and it is a matrix in the cluster-site and spin indices. Using Eq. (A17), switching to Matsubara frequencies and introducing appropriate source fields, we can easily derive the following relations:

$$G_{\text{CPT}} = V^{-1} + V^{-1} G_{\text{aux}} V^{-1} \quad (\text{A18})$$

where G_{aux} and G_{CPT} denote the Ψ 's and Γ 's Green's functions. Eventually, using $G_{\text{aux}} = -(V^{-1} + G_{\text{loc}})^{-1}$ we get the fundamental equation of CPT for the electronic Green's function:

$$G_{\text{CPT}} = (G_{\text{loc}}^{-1} + V)^{-1}. \quad (\text{A19})$$

3. Lattice spectral function

Up to this point spin-indices played the same role as cluster-site indices and the effect of Rashba coupling was considered only in the partitioning of the Hamiltonian.

the auxiliary Grassman fields, Ψ_m and Ψ_m^* . By doing so we obtain

The spin structure of the Green's function becomes relevant again when we use CPT to extract physical information on the lattice ground-state.

Before proceeding further we notice that for single-site cluster the above expression reduces to Hubbard I approximation for the single-particle Green's function. Within this approximation the self-energy is independent of spin and momentum and the interacting spectrum consists of four bands with dispersion

$$\xi_{\mathbf{k}\lambda\nu} = \frac{U + E_{\mathbf{k}\lambda} + \nu \sqrt{U^2 + E_{\mathbf{k}\lambda}^2}}{2} \quad (\text{A20})$$

where the index $\nu = \pm$ identifies the upper and lower Hubbard band while the index $\lambda = \pm$ indicates the helicity with $E_{\mathbf{k}\lambda}$ denoting the dispersion of the helical bands in the absence of interaction,

$$E_{\mathbf{k}\lambda} = \epsilon_0(\mathbf{k}) + 2\lambda t_R \sqrt{\sin^2 k_x + \sin^2 k_y}, \quad (\text{A21})$$

where we defined $\epsilon_0(\mathbf{k}) = -2t [\cos(k_x) + \cos(k_y)]$ and we set $a_x = a_y = 1$.

For finite-size clusters, the different components of the Green's function G_{CPT} are identified by three pairs of indices, (m, n) , (a, b) and (σ, σ') , referring respectively to the position of the cluster and the position and the spin of the electron in the cluster. In order to arrive to a practical expression for the spectral function of the original lattice model starting from G_{CPT} , we switch to momentum space, setting

$$\hat{G}_{\text{CPT}}(\mathbf{k}, \mathbf{k}') = \frac{1}{L} \sum_{a,b,m,n} G_{\text{CPT}} e^{i(\mathbf{k}(\mathbf{r}_m + \mathbf{r}_a) - \mathbf{k}'(\mathbf{r}_n + \mathbf{r}_b))} \quad (\text{A22})$$

where \mathbf{k} and \mathbf{k}' belong to the Brillouin zone of Z_γ . Since CPT preserves the superlattice periodicity, the sum over m, n is straightforward and it yields:

$$G(\mathbf{k}, \mathbf{k}') = \frac{1}{L_c} \sum_{a,b} \sum_{\mathbf{K}} \delta(\mathbf{k} - \mathbf{k}' - \mathbf{K}) g(\omega, \mathbf{k}) e^{i(\mathbf{k}\mathbf{r}_a - \mathbf{k}'\mathbf{r}_b)} \quad (\text{A23})$$

where K belongs to the reciprocal superlattice and $g(\omega, \mathbf{k})$ is the CPT Green's function in the mixed representation defined by Eq. (8) of Section II.

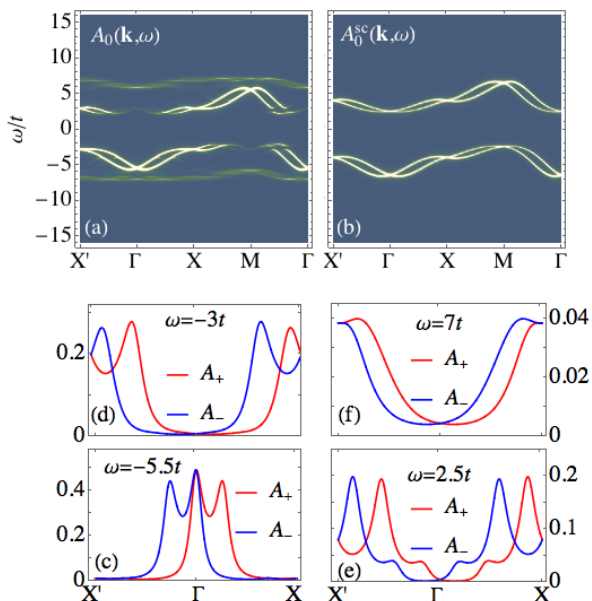


FIG. 7: (a) Spectral function, A_0 , of the Hamiltonian H obtained from CPT for $t_R = 0.5t$, $U = 8t$ and small Lorentzian broadening $\eta = 0.1t$ plotted as a function of energy and momentum across the high-symmetry points: $\Gamma = (0, 0)$, $M = (\pi, \pi)$, $X = (\pi, 0)$, $X' = (-\pi, 0)$. (b) Spectral function obtained from the strong coupling expansion (Eq.(A20)) (c-g) Spin-resolved components of the spectral function along the axis k_x , $A_{\pm}(\omega, \mathbf{k}) = A_0(\omega, \mathbf{k}) \pm A_y(\omega, \mathbf{k})$, for different values of ω . Parameters values as in (a).

Following Ref.[34], we eventually restore the periodicity of the original lattice by keeping only terms with $\mathbf{k} = \mathbf{k}'$ thus defining the Green's function as

$$G_{\sigma\sigma'}(\omega, \mathbf{k}) = \frac{1}{L_c} \sum_{a,b} g_{ab\sigma\sigma'}(\omega, \mathbf{k}) e^{i\mathbf{k}(\mathbf{r}_a - \mathbf{r}_b)} \quad (\text{A24})$$

where we restored the spin indices. Comparing Eqs.(A23) and (A24), one realizes that the periodization prescription of Ref.34 can be interpreted as neglecting Umklapp scattering on the cluster superlattice.

A preliminary understanding of the effects included in CPT can be gained by looking at Fig. 7(a-b) where we compare the CPT spectral function, $A_0(\omega, \mathbf{k})$ to that obtained using the Hubbard I approximation, $A_0^{\text{HI}}(\omega, \mathbf{k})$, the latter yields a good qualitative description of the overall structure of the spectrum at small t_R/t , but, featuring a local spin-independent self-energy, it does not capture the dependence of the spectral weights on \mathbf{k} and on the spin. We notice that in the large U small t_R limit, a weak spin-orbit coupling induces a finite helical spin-polarization in the paramagnetic Mott insulator. This is apparent in Fig. 7(c-g), where we plot the spin-resolved spectral function, $A_{\pm}(\omega, \mathbf{k})$, at different energies for $k_y = 0$ and $k_x \in [-\pi, \pi]$. For these \mathbf{k} -values the RSOC behaves as an effective \mathbf{k} -dependent magnetic field pointing along the y axis and the Green's function can be easily

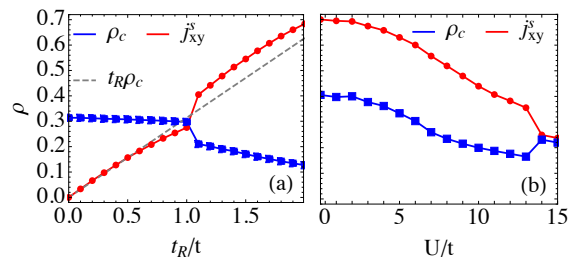


FIG. 8: (a) Bond-charge and spin-current as a function of t_R/t for $U = 15t$, the dashed line represents the product $\rho_c t_R$. (b) Bond-charge and spin-current as a function of U for $t_R = 1.2t$

diagonalized yielding $A_{\pm}(\omega, \mathbf{k}) = A_0(\omega, \mathbf{k}) \pm A_y(\omega, \mathbf{k})$ for the two helicities.

We remark that, for the standard Hubbard model, a variety of papers have shown that CPT gives a proper account of the most important features of the model. In spite of the small clusters size, the plaquette-perturbation-theory approach used in the present work yields results for the gap that approximately agree with those found using larger 4×4 cluster, see e.g. Refs. [52,53].

It is interesting to note that the choice of squared clusters and the periodization scheme proposed in Eq. (A24), preserving the symmetries of the original square lattice, correctly yield a vanishing spin-Hall current, *i.e.*

$$j_s^z = \int d\omega \sum_{\mathbf{k}} \text{Tr} [A(\omega, \mathbf{k}) \sigma_z] \sin(\mathbf{k} \mathbf{a}_\mu) = \mathbf{0} \quad (\text{A25})$$

with $A(\omega, \mathbf{k})$ denoting the spin-dependent spectral function $A_{\sigma\sigma'}(\omega, \mathbf{k}) = -1/\pi \text{Im} [G_{\sigma\sigma'}(\omega, \mathbf{k})]$. The bond-charge, ρ_c ,

$$\rho_c = \sum_{\mathbf{k}} \int A_0(\omega, \mathbf{k}) \cos(k_x) d\omega,$$

and the in-plane equilibrium spin-current,³⁷ j_{xy}^s ,

$$j_{xy}^s = -\frac{1}{2\pi} \sum_{\mathbf{k}} \int_{-\infty}^{\infty} \text{Im} [\text{Tr} [G(\omega, \mathbf{k}) \sin(k_x) \sigma_y]] d\omega,$$

have instead a non-trivial dependence on U and t_R as we show in Fig. 8(a-b). We see that in the AF phase j_{xy}^s grows linearly as a function of t_R while the bond-charge is roughly constant, for a certain value of t_R corresponding to $j_{xy}^s = \rho_c$, the system undergoes the AF-HL transition. The transition yields a strong reduction of the bond charge and a strong increase of the spin-current, indeed due to Pauli principle standard tunneling is suppressed by ferromagnetic correlations while Rashba tunneling is enhanced.

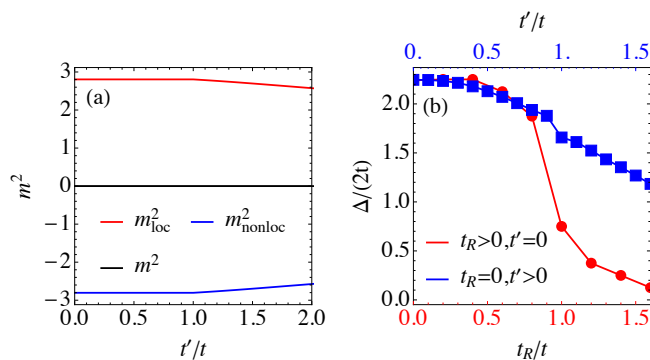


FIG. 9: (a) Local, non-local and total single-cluster magnetic moment at $U = 8t$, $t_R = 0$ as a function of next-nearest-neighbor tunneling. (b) Spectral gap at $U = 8t$ in the extended Hubbard model and in the Rashba-Hubbard model. The value $U = 8t$ is chosen to have the transition in the Rashba-Hubbard model around $t_R \sim t$.

Appendix B: Rashba versus next-nearest neighbor tunneling

In this appendix, we elucidate the peculiarity of Rashba SOC as compared to next-nearest neighbor tunneling, focusing in particular on the behavior of the charge gap. We thus replace the RSOC term in Hamiltonian H_0 , (Eq.(3)) with a next-nearest-neighbor term defined as

$$H_{NN} = -t' \sum_{\langle\langle ij \rangle\rangle} (c_{i\sigma}^\dagger c_{j\sigma} + H.c.)$$

and we use CPT to calculate the spectral function and the charge gap. At a mean field level, Rashba spin-orbit coupling and next-nearest neighbor tunneling, t' , have indeed similar consequences on the density of states of electrons in a two-dimensional square lattice. Both these single-particle terms, break the perfect nesting of the Fermi surface shifting the van Hove singularity its usual location. They also have similar effects on the ground-state of a single plaquette. Indeed, while for a standard Hubbard Hamiltonian, at finite U and t , the plaquette's ground state has d -symmetry, in the presence of Rashba spin-orbit coupling²⁷ or next-nearest neighbors tunneling,⁵¹ it undergoes a transition to a state with s -symmetry.

In spite of these similarities, CPT yields very different spectral properties for the Rashba-Hubbard model and the Hubbard model with next-nearest-neighbor tunneling.

In particular, as shown in Figure 9(a) t' has a weak effect on the magnetic moment of the plaquette and the non-local magnetization remain always negative indicating AF correlation. By looking at the gap behavior, we can distinguish two regimes: in the first regime t' has roughly the same effect of t_R ; this is the regime where the ground state of the Rashba-Hubbard model is mostly a singlet. In the second regime, for $t' > t$ the bandwidth of the extended Hubbard model starts to increase with increasing t' , as one can see, however this has a much weaker effect on the gap as compared to the screening induced by RSOC in the triplet ground-state.

¹ L. P. Gorkov and E. I. Rashba, Phys. Rev. Lett. **87**, 037004 (2001).

² M.H. Fischer, M. Sigrist, and D. F. Agterberg, Phys. Rev. Lett. **121**, 157003 (2018).

³ F. Hellman, A. Hoffmann, Y. Tserkovnyak, G. S. D. Beach, E. E. Fullerton, C. Leighton, A. H. MacDonald, D. C. Ralph, D. A. Arena, H. A. Dürr, P. Fischer, J. Grollier, J. P. Heremans, T. Jungwirth, A. V. Kimel, B. Koopmans, I. N. Krivorotov, S. J. May, A. K. Petford-Long, J. M. Rondinelli, N. Samarth, I. K. Schuller, A. N. Slavin, M. D. Stiles, O. Tchernyshyov, A. Thiaville, and B. L. Zink, Rev. Mod. Phys. **89**, 025006 (2017).

⁴ C. W. J. Beenakker, Rev. Mod. Phys. **69**, 731 (1997).

⁵ V. Brosco, M. Jerger, P. San-José, G. Zarand, A. Shnirman, and G. Schön, Phys. Rev. B **82**, 041309(R) (2010).

⁶ C. Gorini, A. Maleki Sheikhabadi, K. Shen, I. V. Tokatly, G. Vignale, and R. Raimondi, Phys. Rev. B **95**, 205424 (2017).

⁷ A. Manchon, H. C. Koo, J. Nitta, S. M. Frolov, and R. A. Duine, Nat. Mater. **14**, 871 (2015).

⁸ R. Winkler, *Spin-Orbit Coupling Effects in Two-Dimensional Electron and Hole Systems* (Springer, Berlin-Heidelberg, 2003).

⁹ C. R. Ast, J. Henk, A. Ernst, L. Moreschini, M. C. Falub, D. Pacilé, P. Bruno, K. Kern, and M. Grioni Phys. Rev.

Let. **98**, 186807 (2007).

¹⁰ Q. Liu, Y. Guo, and A. J. Freeman, Nano Lett. **13**, 5264 (2013).

¹¹ C. Tresca, C. Brun, T. Bilgeri, G. Menard, V. Cherkez, R. Federicci, D. Longo, F. Debontridder, M. D'angelo, D. Roditchev, G. Profeta, M. Calandra, and T. Cren, Phys. Rev. Lett. **120**, 196402 (2018).

¹² E. I. Rashba, Phys. Rev. B **86**, 125319 (2012).

¹³ A. Generalov, M. M. Otrokov, A. Chikina, K. Kliemt, K. Kummer, M. Höppner, M. Güttler, S. Seiro, A. Fedorov, S. Schulz, and et al., Nano Lett. **17**, 811 (2017).

¹⁴ K. Ishizaka, M. S. Bahramy, H. Murakawa, M. Sakano, T. Shimojima, T. Sonobe, K. Koizumi, S. Shin, H. Miyahara, A. Kimura, and et al., Nat. Mat. **10**, 521 (2011).

¹⁵ J. Nitta, T. Akazaki, H. Takayanagi, and T. Enoki, Phys. Rev. Lett. **78**, 1335 (1997).

¹⁶ A. D. Caviglia, M. Gabay, S. Gariglio, N. Reyren, C. Cancellieri, and J.-M. Triscone, Phys. Rev. Lett. **104**, 126803 (2010).

¹⁷ D. Santos-Cottin, M. Casula, G. Lantz, Y. Klein, L. Petaccia, P. Le Fevre, F. Bertran, E. Papalazarou, M. Marsi, and A. Gauzzi, Nat. Comm. **7**, 11258 (2016).

¹⁸ V. Baltz, A. Manchon, M. Tsoi, T. Moriyama, T. Ono, and Y. Tserkovnyak, Rev. Mod. Phys. **90**, 015005 (2018).

¹⁹ T. Jungwirth, J. Sinova, A. Manchon, X. Marti, J. Wun-

- derlich, and C. Felser, Nat. Phys. **14**, 200 (2018).
- ²⁰ E. I. Rashba and V. I. Sheka, Fiz. Tverd. Tela: Collected Papers **2**, 162 (1959).
- ²¹ X. Zhang, W. Wu, G. Li, L. Wen, Q. Sun, and A.-C. Ji, New J. of Phys. **17**, 073036 (2015).
- ²² A. Farrell and T. Pereg-Barnea, Phys. Rev. B **89**, 035112 (2014)
- ²³ M. Laubach, J. Reuther, R. Thomale, and S. Rachel, Phys. Rev. B **90**, 165136 (2014).
- ²⁴ P. Rosenberg, H. Shi, and S. Zhang, Phys. Rev. Lett. **119**, 265301 (2017).
- ²⁵ A. Ashrafi and D. L. Maslov, Phys. Rev. Lett. **109**, 227201 (2012).
- ²⁶ A. Ashrafi, E. I. Rashba, and D. L. Maslov, Physical Review B **88**, 075115 (2013).
- ²⁷ V. Brosco, D. Guerci, and M. Capone, Phys. Rev. B **97**, 125103 (2018).
- ²⁸ V. Brosco, L. Benfatto, E. Cappelluti, and C. Grimaldi, Phys. Rev. Lett. **116**, 166602 (2016).
- ²⁹ V Brosco, C Grimaldi, E Cappelluti, L Benfatto, Journal of Physics and Chemistry of Solids **128**, 152 (2019)
- ³⁰ V. Brosco and C. Grimaldi, Phys. Rev. B **95**, 195164 (2017).
- ³¹ Y.-Y. Pai, A. Tylan -Tyler, P. Irvin, and J. Levy, Rep. Progr. Phys. **81**, 036503 (2018).
- ³² M. H., H. Bentmann, C. Seibel, C. Tusche, S. V. Ere-meev, T. R. F. Peixoto, O. E. Tereshchenko, K. A. Kokh, E. V. Chulkov, J. Kirschner, and F. Reinert, Nat. Comm. **7**, (2016).
- ³³ D. Sénéchal, D. Perez, and M. Pioro-Ladrière, Phys. Rev. Lett. **84**, 522 (2000).
- ³⁴ D. Sénéchal, D. Perez, and D. Plouffe, Phys. Rev. B **66**, 075129 (2002).
- ³⁵ S. Pairault, D. Sénéchal, and A.-M. S. Tremblay, Phys. Rev. Lett. **80**, 5389 (1998).
- ³⁶ E. H. Phys. Rev. Lett. **62**, 1201 (1989).
- ³⁷ E.I. Rashba, Phys. Rev. B **68**, 241315(R) (2003).
- ³⁸ The “HL” and “AF” insulating phase may display complex magnetic textures that are not the focus of the present work, see e.g. [22].
- ³⁹ More details on on the non-interacting band structure justifying the expression of t_{eff} may be found in appendix A 3.
- ⁴⁰ A. Isidori, M. Berovič, L. Fanfarillo, L. de Medici, M. Fabrizio, and M. Capone Phys. Rev. Lett. **122**, 186401 (2019).
- ⁴¹ L. Laloux, A. Georges, and W. Krauth Phys. Rev. B **50**, 3092 (1994).
- ⁴² K. Gotlieb, Chiu-Yun Lin, M. Serbyn, W. Zhang, C. L. Smallwood, C. Jozwiak, H. Eisaki, Z. Hussain, A. Vishwanath, and A. Lanzara, Science **362**, 1271 (2018).
- ⁴³ M. Civelli, M. Capone, S. S. Kancharla, O. Parcollet, and G. Kotliar, Phys. Rev. Lett. **95**, 106402 (2005).
- ⁴⁴ M. Civelli, M. Capone, A. Georges, K. Haule, O. Parcollet, T. D. Stanescu, and G. Kotliar, Phys. Rev. Lett. **100**, 046402 (2008).
- ⁴⁵ G. Profeta and E. Tosatti, Phys. Rev. Lett. **98** 086401 (2007).
- ⁴⁶ E. Cappelluti, C. Grimaldi, and F. Marsiglio, Phys. Rev. Lett. **98**, 167002 (2007).
- ⁴⁷ S. Pairault, D. Sénéchal, and A.-M. S. Tremblay, Eur. Phys. J. B. **16**, 85 (2000).
- ⁴⁸ S. K. Sarker J. Phys. C **21**, L667 (1988).
- ⁴⁹ M. Pothoff, Lecture Notes of the Autumn School on Correlated Electrons, “DMFT at 25: Infinite Dimensions”, (Forschungszentrum Jülich, 2014).
- ⁵⁰ J. W. Negele, H. Orland *Quantum theory of many particle systems* (Perseus Books, 1998).
- ⁵¹ H. Yao and S. A. Kivelson, Phys. Rev. Lett. **105**, 166402 (2010).
- ⁵² M. Kohno, Phys. Rev. Lett. **108**, 076401 (2012).
- ⁵³ M. Kohno, Phys. Rev. B **90**, 035111 (2014).